

Article

Catalytic Performance of Alumina-Supported Cobalt Carbide Catalysts for Low-Temperature Fischer–Tropsch Synthesis

Zahra Gholami ^{1,*}, Zdeněk Tišler ¹, Eliška Svobodová ¹, Ivana Hradecká ¹, Nikita Sharkov ¹ and Fatemeh Gholami ²

¹ ORLEN UniCRE, a.s., 436 70 Litvínov, Czech Republic

² New Technologies-Research Centre, University of West Bohemia, 301 00 Plzeň, Czech Republic

* Correspondence: zahra.gholami@orlenunicre.cz; Tel.: +420-731-576-893

Abstract: The determination of the catalyst's active phase helps improve the catalytic performance of the Fischer–Tropsch (FT) synthesis. Different phases of cobalt, including cobalt oxide, carbide, and metal, exist during the reaction. The content of each phase can affect the catalytic performance and product distribution. In this study, a series of cobalt carbide catalysts were synthesized by exposure of Co/Al₂O₃ catalyst to CH₄ at different temperatures from 300 °C to 800 °C. The physicochemical properties of the carbide catalysts (CoC_x/Al₂O₃) were evaluated by different characterization methods. The catalytic performances of the catalysts were investigated in an autoclave reactor to determine the role of cobalt carbides on the CO conversion and product distribution during the reaction. XRD and XPS analysis confirmed the presence of Co₂C in the prepared catalysts. The higher carbidation temperature resulted in the decomposition of methane into hydrogen and carbon, and the presence of graphitic carbon was confirmed by XRD, XPS, SEM, and Raman analysis. The Co₂C also decomposed to metallic cobalt and carbon, and the content of cobalt carbide decreased at higher carbidation temperatures. Higher content of Co₂C resulted in a lower CO conversion and higher selectivity to light alkanes, mainly methane. The higher carbidation temperature resulted in the decomposition of Co₂C to metallic cobalt with higher activity in the FT reaction. The CO conversion increased by increasing the carbidation temperature from 300 °C to 800 °C, due to the higher content of metallic cobalt. In the presence of pure hydrogen, the Co₂C could be converted mainly into hexagonal, close-packed (hcp) Co with higher activity for dissociative adsorption of CO, which resulted in higher catalyst activity and selectivity to heavier hydrocarbons.

Keywords: Fischer–Tropsch; cobalt carbide; active phase; product distribution; metallic cobalt



Citation: Gholami, Z.; Tišler, Z.; Svobodová, E.; Hradecká, I.; Sharkov, N.; Gholami, F. Catalytic Performance of Alumina-Supported Cobalt Carbide Catalysts for Low-Temperature Fischer–Tropsch Synthesis. *Catalysts* **2022**, *12*, 1222. <https://doi.org/10.3390/catal12101222>

Academic Editors: Fanhui Meng and Wenlong Mo

Received: 27 September 2022

Accepted: 10 October 2022

Published: 12 October 2022

Publisher's Note: MDPI stays neutral with regard to jurisdictional claims in published maps and institutional affiliations.



Copyright: © 2022 by the authors. Licensee MDPI, Basel, Switzerland. This article is an open access article distributed under the terms and conditions of the Creative Commons Attribution (CC BY) license (<https://creativecommons.org/licenses/by/4.0/>).

1. Introduction

Fischer–Tropsch (FT) synthesis is a well-known catalytic process for the production of sulfur and aromatic-free fuels and other value-added chemicals from syngas. Through FT synthesis, which is a catalytic polymerization reaction, syngas is converted to a wide range of products, such as paraffins, olefins, and alcohols. The catalytic performance and product distribution are directly affected by the type of catalyst and its chemical composition and structure. The elements of groups 8–10 of the periodic table with good ability for adsorption and dissociation of CO and H₂ are reported as active metals for the FT reaction, whereas iron and cobalt are the most commonly used catalysts for this reaction [1–4]. Cobalt-based catalysts with higher stability, more resistance to deactivation, lower water–gas shift activity, and high hydrocarbon productivity were considered the ideal choice for synthesizing long-chain hydrocarbons at moderate temperatures and pressures [5,6].

During the FT reaction over CO-based catalysts (which typically proceeds at 220–250 °C, 20 bar, and an H₂/CO ratio of two), the chain growth and propagation of hydrocarbons mainly occurred on cobalt metal sites. Cobalt oxide and cobalt carbide, which are formed by re-oxidation and carburization of the metal catalyst during the FT synthesis, are known

as inactive cobalt components in FT synthesis, and they are often considered deactivation signs [2,5,7,8]. However, some other groups reported that cobalt carbides could enhance the selectivity to lower olefins [9–11]; they also act as an active site for a water–gas shift reaction and oxygenates production [12–14] or act as an intermediate reacts with hydrogen to form methylene, acting as a chain-growth monomer for the formation of long-chain hydrocarbons [15]. However, unlike the cobalt catalysts, during the FT synthesis over iron-based catalysts, the Hägg carbide (χ -Fe₅C₂), as the real active phase, plays the main role in catalytic performances [8,16]. The presence of cobalt carbide phases during the FT synthesis could affect the CO conversion and product selectivity [17].

However, Co₂C is often known as an inactive component in FT synthesis via Co-based catalysts, but Co₂C content, their different morphologies, and the form of the Co₂C phase could have different effects on the catalytic performance of Co-based catalysts during the FT reaction. The Co₂C(111) facet is ascribed to the nanosphere-like particles with lower activity and higher methane selectivity under mild FT reaction conditions [10,13,18]. Co₂C nanoprisms with specific exposed facets of (101) and (020), as the FTO active phase, showed a higher intrinsic activity for CO hydrogenation and a lower methane selectivity [9,10,18]. The presence of Co⁰ resulted in a lower CO₂ and methane selectivity and higher selectivity to longer-chain hydrocarbons. The Co₂C was reported to be relatively stable under FT reaction conditions [5,19]. At the same time, it was reported that the cobalt carbides appear to be unstable and can be decomposed to metallic cobalt and carbon during the FT reaction, especially at higher reaction temperatures and lower H₂/CO ratio [1,3,20].

In the present study, a series of CoC_x/Al₂O₃ catalysts were synthesized by carburization of Co/Al₂O₃ catalysts using methane at different temperatures from 300 °C to 800 °C. The properties of these catalysts changed according to their carburization temperatures. Changing the carburization temperature could result in the formation of different content and types of cobalt phases, which can alter their catalyst activity and product selectivity during the FT reaction. The physicochemical properties of the catalysts were investigated by different characterization methods, including scanning electron microscopy (SEM), X-ray diffraction (XRD), X-ray photoelectron spectroscopy (XPS), and Raman analysis. The catalytic performances of the catalysts were evaluated in an autoclave reactor to determine the role of cobalt carbides on the CO conversion and product distribution during the reaction.

2. Results and Discussion

2.1. Catalyst Characterization

SEM images (Figure 1) of the prepared CoC_x/Al₂O₃ catalysts at different temperatures confirmed the formation of carbon fibers on the surface after the decomposition of methane at higher temperatures. The formation of carbon at lower temperatures was not detected in SEM images, but the carbon fibers can be seen on the surface of catalysts at high temperatures of 700 °C and 800 °C, which was in good accordance with the obtained results in XRD and elemental analysis results.

The peaks belonging to Al₂O₃ at ~37.5°, 46.1°, 56°, and 67° (JCPDS 10-0425) were observed in the XRD patterns of all prepared catalysts (Figure 2a) [21–24]. The peaks at 37.0°, 41.3°, 42.5°, 45.7°, and 56.6° can be assigned to the Co₂C crystalline plane (110), (002), (111), (021), and (112), (JCPDS 65-1457) [3,9,10,19,25,26] respectively. However, the peak at 56.6° was not very visible in the XRD patterns shown in Figure 1a. The cobalt carbide decomposition to graphitic carbon and metallic cobalt (Co₂C → Co + C) was started at temperatures above 275 °C [5,27,28], and it could be the reason for gradually decreasing the cobalt carbide and increasing the metallic cobalt by increasing the temperature. In addition, in the presence of Co/Al₂O₃ catalyst, methane also can be decomposed directly to hydrogen and carbon (CH₄ → 2H₂ + C) [29–33]. At high temperatures (above 600 °C), due to the decomposition of methane, the concentration of graphitic carbon also significantly increased, as shown by the XRD spectra of the catalysts. Decomposition of methane on cobalt catalysts led to the formation of fcc cobalt [34]. The peak at 26.3° (graphite, JCPDS 41-

1478) and 51.5° (fcc Co, JCPDS 1-1255) [35,36] were observed only in the sample prepared at a temperature above 600°C . The peak at 44.3° was very weak for the samples prepared at low temperatures, and the peak's intensity increased by increasing the temperature. These peaks can belong to both fcc Co (111) (JCPDS 1-1255) and graphitic carbon (JCPDS 41-1478) [3,9,36], which could be formed due to the reduction of cobalt oxide to Co (fcc) during the catalysts' carbidation in the presence of 20%CH₄ in H₂. By increasing the carbidation temperature, the intensity of fcc Co increased, whereas the intensity of the Co₂C(111) facet (at 2θ of 42.5°) decreased. The Co₂C(111) facet is responsible for lower CO hydrogenation and higher CH₄ selectivity during the FT synthesis under mild reaction conditions.

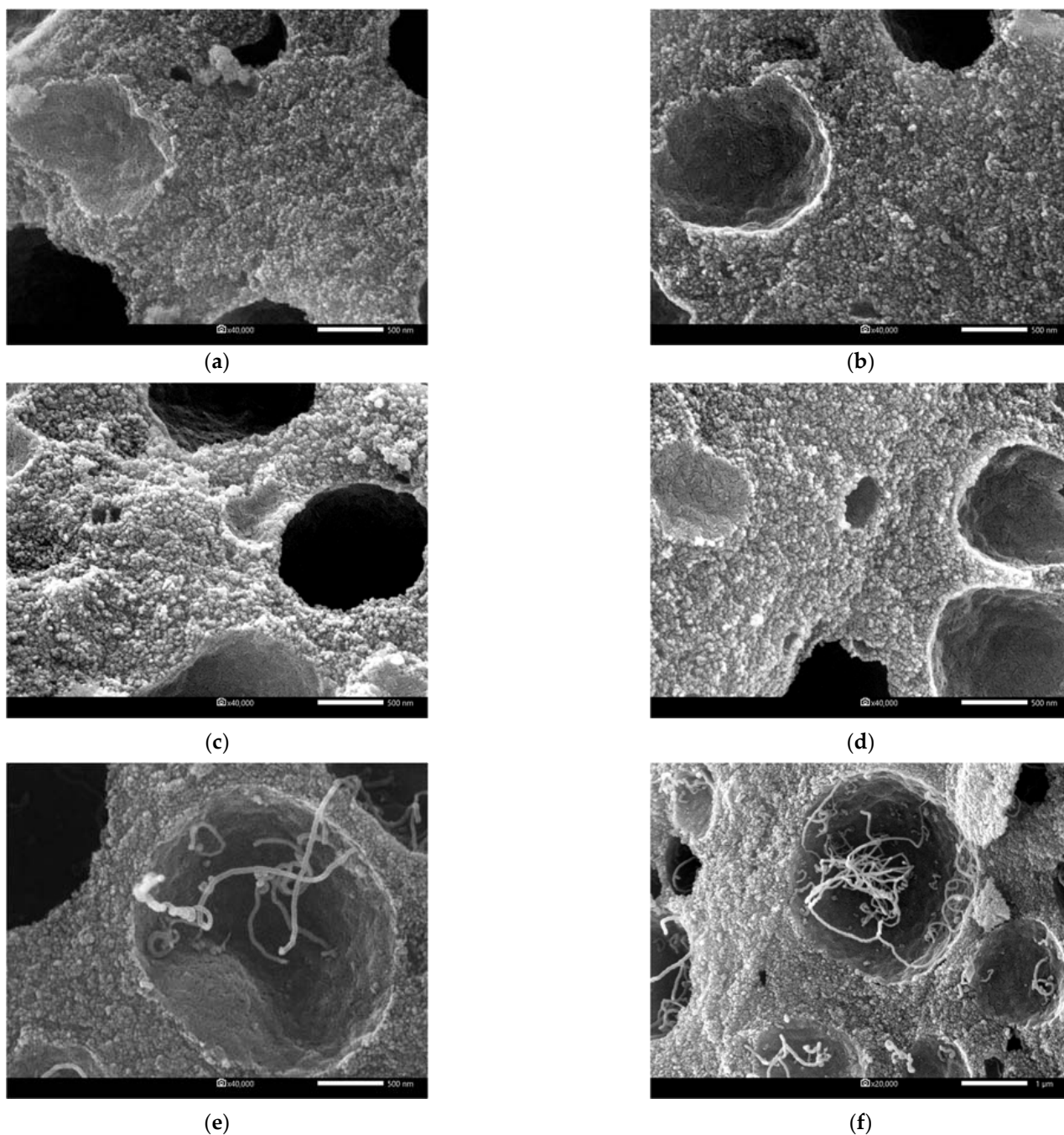


Figure 1. SEM images of the 5CoC_x/Al₂O₃ catalysts prepared at different temperatures, (a) 300°C , (b) 400°C , (c) 500°C , (d) 600°C , (e) 700°C , (f) 800°C .

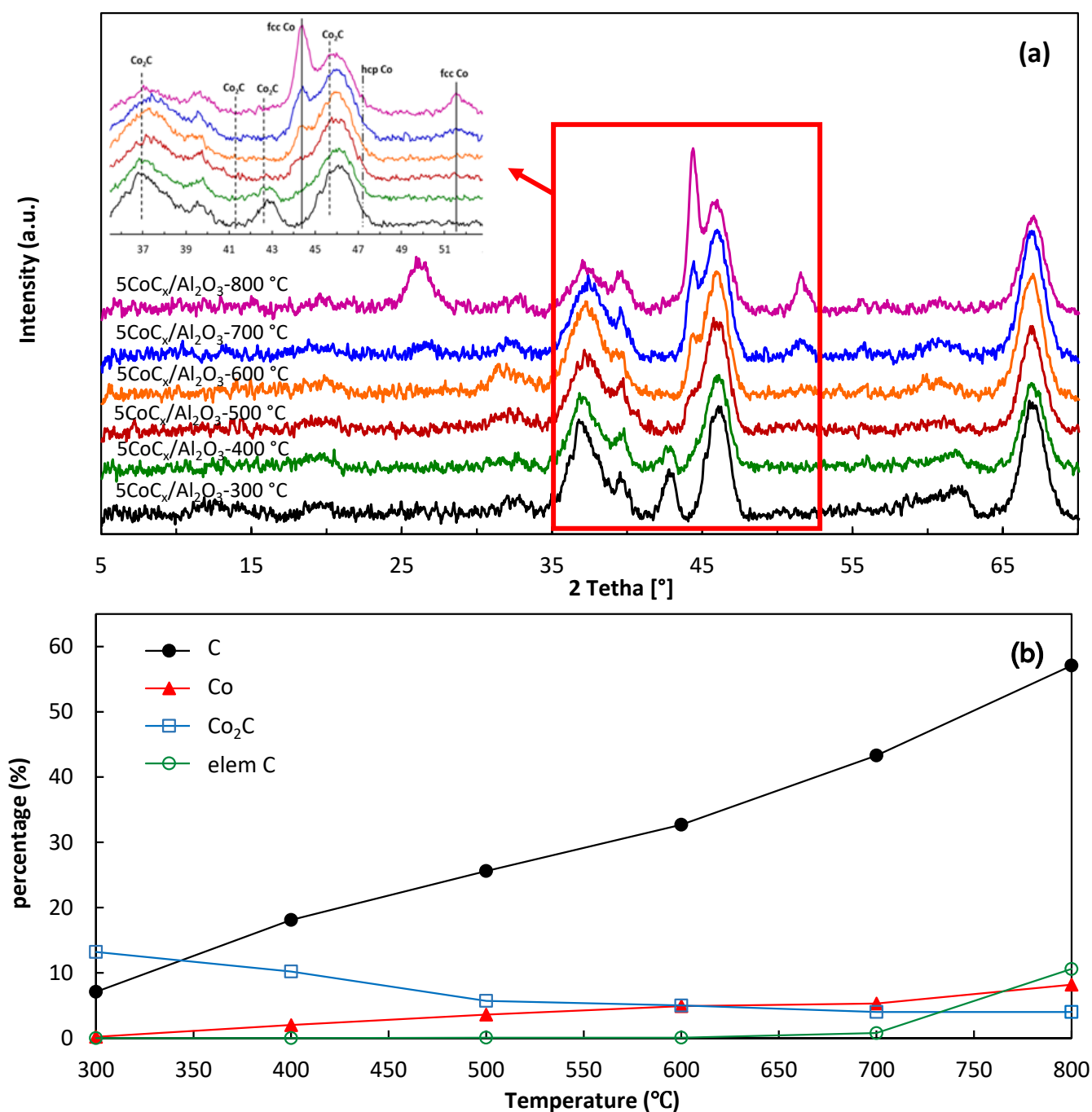


Figure 2. (a) XRD patterns of $5\text{CoC}_x/\text{Al}_2\text{O}_3$ and catalysts prepared at different temperatures, (b) Content of individual phases according to SQ performed from XRD spectra (C-carbon, Co-cobalt, Co_2C -carbide) and carbon content determined by elemental analysis (elemC).

The contents of phases of C (carbon), Co (cobalt), and Co_2C (cobalt carbide) were detected from the XRD results and semi-quantitative (SQ) evaluation, and the carbon content (elemental C) of the prepared samples was also measured using elemental analysis (Figure 2b). Decomposition of methane at higher temperatures increased the carbon content on the surface of the prepared catalysts. By increasing the temperature, the formed Co_2C became unstable and decomposed to C and metallic Co, and its content decreased [5,27,28]. Decomposition of cobalt carbide to graphitic carbon and hydrogen is started at temperatures above 275 °C; however, in the presence of hydrogen, it could happen at lower temperatures [5,27,37]. The XRD pattern (Figure 2a) showed that the intensity of the peaks

belonging to the Co_2C decreased gradually by increasing the temperature from 300 °C to 800 °C [19]. Elemental analysis of the carbon (Figure 2b) also confirmed that an increase in the temperature led to the formation of more carbon. Cobalt carbides were unstable at high temperatures; they decomposed to metallic cobalt and carbon at high temperatures. However, due to the overlapping of the carbon and cobalt peaks, with the similar cubic structure, it was difficult to accurately distinguish between the two phases in XRD patterns. XPS analysis was performed for further investigation and evaluation of the active phases of the catalysts.

XPS analysis was used to investigate the chemical composition and elemental oxidation states of the catalysts. The survey scan of carbide catalysts is shown in Figure S1, which confirmed the existence of C, O, Co, and Al in these prepared catalysts. The intensity of C 1s peaks increased by increasing the temperature, whereas the intensity of Co 2p peaks decreased. The strong C 1s peak observed at about 284.6 eV was ascribed to sp^2 elemental carbon (C-C), such as carbon fibers or carbon nanotubes [38]. The high intensity of this peak in the C 1s spectra (Figure 3a) of the catalysts prepared at higher temperatures (800 °C and 700 °C) was due to the presence of graphitic carbon, as confirmed by SEM, XRD, and Raman analysis. The Co-C peak at around 283.1 eV followed the reverse trend. By increasing the temperature of carbidation, the content of Co-C decreased. In addition to the C-C and Co-C bonds, other bonds at 286.5 eV and 288.5 eV were attributed to the O-C-O and O=C-O bonds, respectively. The $\pi \rightarrow \pi^*$ shake-up satellite peak was also observed at about 291.2 eV. The obtained results are in good agreement with the reported results where the Co-C bonds were C-Co bonds; these were detected, confirming the presence of Co_2C in the prepared catalysts [39,40].

XPS spectra of Co 2p (Figure 3b) showed that the bond at about 778.6 eV was attributed to the Co^{2+} of carbidic Co of the prepared catalysts. The intensity of the Co-C bond decreased by the carbidation temperature, whereas the intensity of peaks belonging to metallic cobalt (Co^0) (at around 782.3 eV) increased at higher temperatures. These findings are in good agreement with the XRD analysis of the catalysts, where the Co_2C content decreased at higher temperatures, and metallic cobalt peaks were detected at higher temperatures. However, by increasing the temperature to above 600 °C and formation of more graphitic carbon on the surface of the catalysts, the intensity of the Co peaks in Co 2p spectra decreased, which is in good accordance with the C 1s spectra of these catalysts, where the content of graphitic carbon increased significantly at high temperatures.

As mentioned earlier, the decomposition of cobalt carbide to cobalt and graphitic carbon started at temperatures above 275 °C [5,27], and this could be the reason for the increase in the $\text{Co}^0/\text{Co-C}$ and $\text{C-C}/\text{Co}^0$ ratios when the carbidation temperature increased (Table 1). However, for the catalyst with the carbidation temperature of 800 °C, the $\text{Co}^0/\text{Co-C}$ ratios decreased compared with that of 700 °C, which could be due to the deposition of graphitic carbon on the catalyst's surface and blockage of metallic cobalt on the surface. The sharp increase in the $\text{C-C}/\text{Co}^0$ at 800 °C was in good agreement with this finding. The XPS analysis of cobalt carbide nanoparticles and nanosheets performed by other research groups also showed similar patterns for cobalt carbides, and the peaks attributed to cobalt carbides were observed at about 283 eV (C 1s) and 778.5 eV (Co 2p 3/2) [26,41,42].

Raman spectroscopy analysis could be beneficial for the investigation of the materials' properties and could provide information about molecular vibrations. Raman spectra of the $\text{Co}/\text{Al}_2\text{O}_3$ catalysts at different carbidation temperatures are shown in Figure 4. The D and G bands belonging to carbon were not clearly observed for the catalysts prepared at the carbidation temperatures in the range of 300 °C to 600 °C. The D and G bands were clearly detected for the catalysts prepared at 700 °C and 800 °C. The peaks at around 1340 cm^{-1} and 1573 cm^{-1} were typical for D and G bands, respectively. The D and G bands of the carbon materials could be observed if amorphous carbon or nanocrystalline graphite existed in a metal carbide matrix [43,44].

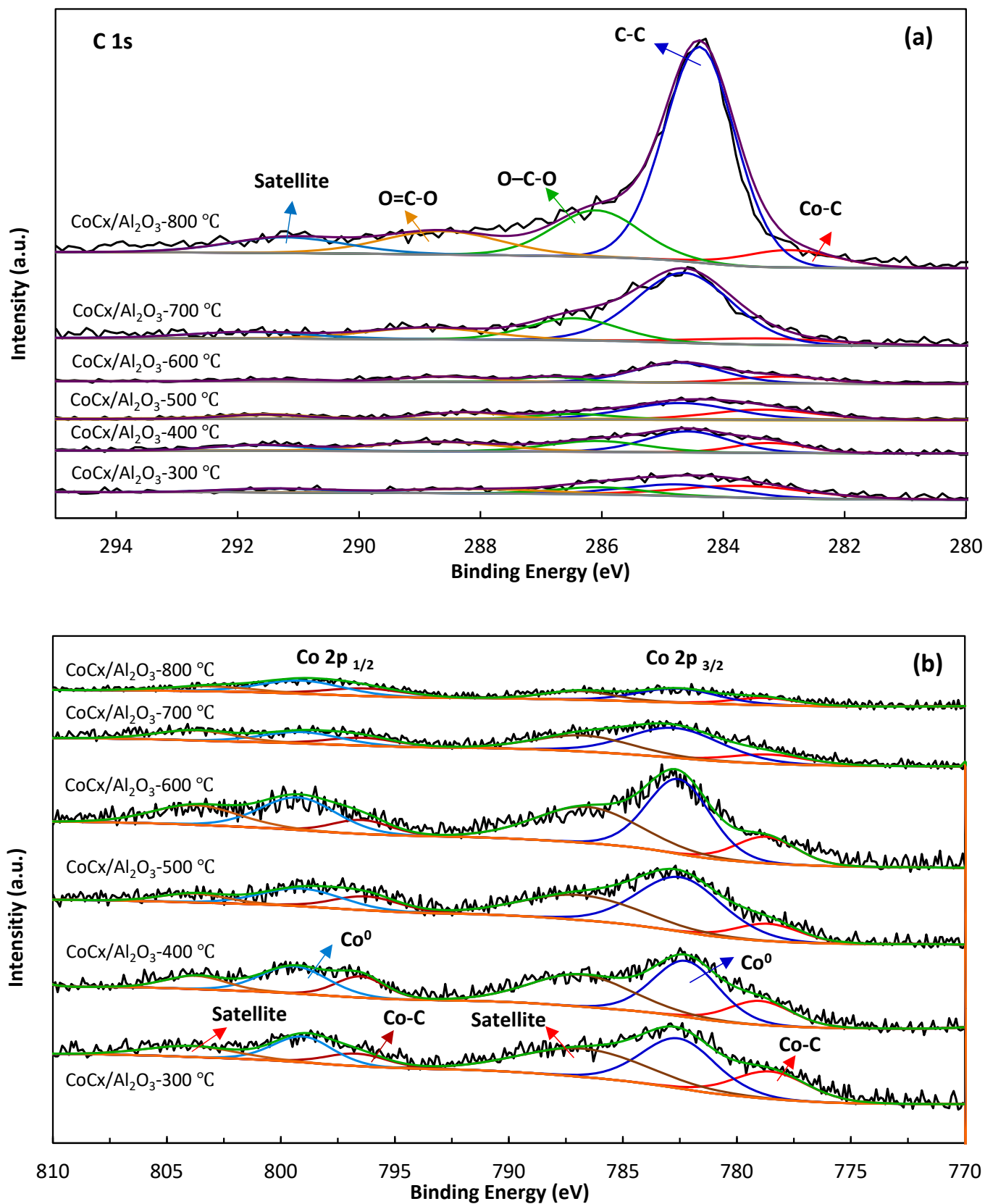
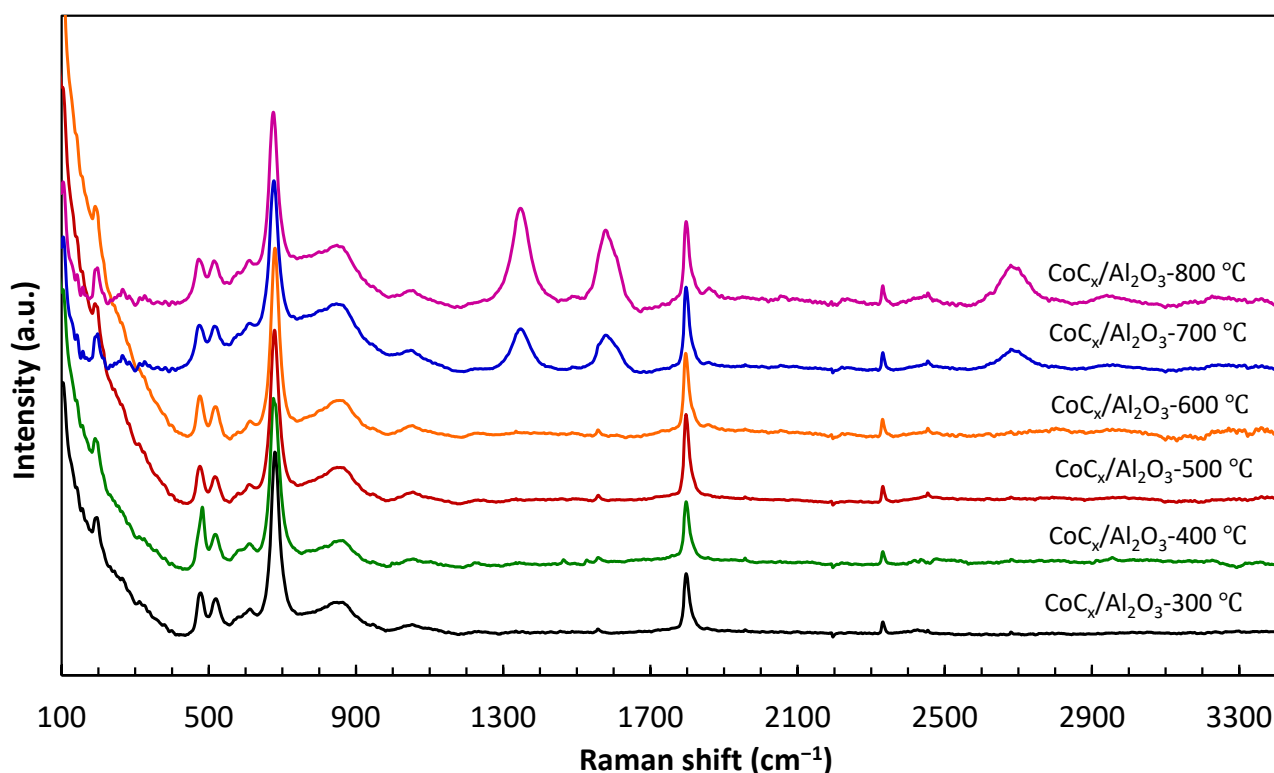


Figure 3. (a) C 1s spectra, and (b) Co 2p spectra of CoC_x/Al₂O₃ catalysts prepared at different temperatures.

Table 1. XPS data analysis of C 1s and Co2p peaks of CoC_x/Al₂O₃ catalysts.

	C 1s			Co 2p	
	Co-C Peak BE (eV)	C-C Peak BE (eV)	C-C/Co-C	Co-C Peak BE (eV)	Co ⁰ /Co-C
CoC _x /Al ₂ O ₃ -300 °C	283.2	284.7	0.63	778.5 (2p _{3/2}) 796.3 (2p _{1/2})	1.68
CoC _x /Al ₂ O ₃ -400 °C	283.3	284.7	1.49	778.6 (2p _{3/2}) 796.4 (2p _{1/2})	2.08
CoC _x /Al ₂ O ₃ -500 °C	283.1	284.5	0.99	778.7 (2p _{3/2}) 796.3 (2p _{1/2})	2.85
CoC _x /Al ₂ O ₃ -600 °C	283.2	284.8	2.36	778.7 (2p _{3/2}) 796.4 (2p _{1/2})	2.67
CoC _x /Al ₂ O ₃ -700 °C	283.3	284.6	6.10	778.5 (2p _{3/2}) 796.7 (2p _{1/2})	2.70
CoC _x /Al ₂ O ₃ -800 °C	283.3	284.4	14.26	778.6 (2p _{3/2}) 796.0 (2p _{1/2})	1.49

**Figure 4.** Raman spectrum of the catalysts prepared at different carbidation temperatures.

The D mode is caused by the disordered structure of graphene, and it originates from the A_{1g} breathing vibrations of the sixfold carbon rings involving phonons near the K zone boundary (Figure S2). The G band, which lies in the range of 1500–1600 cm⁻¹, is ascribed to the graphitic carbon with E_{2g} symmetry that involves the in-plane bond-stretching vibration of sp² carbon sites. This mode does not require the presence of sixfold rings, so it occurs at all sp² sites, not only those in the rings [45,46]. It is worth mentioning that the G mode is due to the relative motion of sp² carbon atoms and can also be found in chains.

As mentioned above, the G peak could be observed in the range of 1500–1600 cm⁻¹. By changing the structure of crystallized graphite to nanocrystalline graphite, the peak shifts to 1600 cm⁻¹, and the peak shifts to 1500 cm⁻¹ for amorphous carbon when a loss of aromatic bonding appears. Thus, it can be confirmed that the G band positions (1573 cm⁻¹)

of the catalysts are close to that of nanocrystalline graphite of nanometer-sized clusters [47]. The degree of crystallinity and graphitization formed carbon on the surface of catalysts after carbidation at 700 °C and 800 °C can be measured by the intensity ratio of I_D/I_G . The higher crystallinity could be observed in catalysts with a lower I_D/I_G ratio (Table 2). In this study, the I_D/I_G decreased from 1.18 to 1.28 by increasing the carbidation temperature from 700 °C to 800 °C, which is not clearly confirming the higher crystallinity of the deposited carbon on the surface of the catalyst prepared at the higher temperature. However, the higher intensities in the catalysts prepared at 800 °C could confirm the higher content of the deposited carbon on the catalyst's surface.

Table 2. Raman spectra for carbonaceous materials observed in the prepared catalysts.

Catalyst	D		G		G'		I_D/I_G
	Peak Position (cm ⁻¹)	Intensity	Peak Position (cm ⁻¹)	Intensity	Peak Position (cm ⁻¹)	Intensity	
CoC _x /Al ₂ O ₃ -300 °C	—	—	—	—	—	—	—
CoC _x /Al ₂ O ₃ -400 °C	—	—	—	—	—	—	—
CoC _x /Al ₂ O ₃ -500 °C	—	—	—	—	—	—	—
CoC _x /Al ₂ O ₃ -600 °C	—	—	—	—	—	—	—
CoC _x /Al ₂ O ₃ -700 °C	1340	18.8	1573	16.0	2677	11.1	1.18
CoC _x /Al ₂ O ₃ -800 °C	1341	45.0	1573	35.1	2677	19.1	1.28

All kinds of sp² carbon materials exhibited a peak in the range 2500–2800 cm⁻¹ in the Raman spectra. The G' band (or 2D band) was also observed at 2677 cm⁻¹. The intensity of the G' band in the prepared catalysts increased by increasing the carbidation temperature. The G' band usually helps discriminate the differences between the layers and loading order of the multi-layer graphene system [48]. The single-layer graphene shows a G' band with high intensity. By increasing the graphite layers, the peak becomes broader. In the catalyst prepared at 800 °C, the intensity of the G' band at around 2677 cm⁻¹ peak increased due to the higher amount of carbon on the catalyst's surface. The catalysts prepared at lower carbidation temperatures (≤600 °C) did not show any peak belonging to graphitic carbon.

The Raman peaks below 700 cm⁻¹ are attributed to the Co-Co stretching mode. The observed peaks for cobalt are very similar to those reported in the Raman spectra of cobalt oxide nanoparticles [49–56]. Five (A_{1g} + E_g + 3 F_{2g}) Raman-active modes were observed and identified. The band at around 187 cm⁻¹ was ascribed to the tetrahedral sites' (CoO₄) characteristics with the F_{2g} mode (Figure. 3b). The bands at 470, 510, and 607 are attributed to the E_g, F_{2g}, and F_{2g} symmetry, respectively. Generally, the E_g and F_{2g} modes were related to the combined vibrations of the tetrahedral site and octahedral oxygen motions. The band at 671 cm⁻¹ with A_{1g} symmetry was attributed to the characteristics of the octahedral sites (CoO₆) [49–54]. D'Ippolito and Andreozzi [56] also reported that the Raman vibrational modes of spinel oxides are generally observed in the range of 100–800 cm⁻¹. Diallo et al. [49], Rashad et al. [50], Jiang and Li [51], and Hadjiev et al. [52] also observed the same Raman bands for the Co₃O₄ nanoparticles. The intensity of the bands in the range of 100–800 cm⁻¹ belonging to Co₃O₄ nanoparticles decreased gradually with increasing carbidation temperature. This phenomenon was more evident in the samples with carbidation temperature above 600 °C, which could be due to the coverage of the surface by deposited carbon. The weak band at around 2330 cm⁻¹, observed in all spectra, could be attributed to the characteristic line of nitrogen from the air [57–59]. The peak at around 1790 cm⁻¹ was ascribed to the carbonyl (C=O) stretch bands [60–63], which could be formed after the passivation of the catalyst under oxygen after carbidation.

2.2. Catalyst Evaluation

The results of the FT reaction in the autoclave reactor are shown in Figures 5 and 6. The FT reactions were first performed using the carbide catalysts without prior reduction (WR) by hydrogen (Figure 5a). The catalyst with higher Co₂C content (300-WR, the catalyst

prepared at the carbidation temperature of 300 °C and used in FT without prior reduction with H₂) showed the lowest CO conversion of about 26%. By increasing the carbidation temperature, the catalyst activity also increased to 74% for the catalyst prepared at 800 °C. As was described earlier, increasing the carbidation temperature resulted in the formation of more metallic cobalt and lower cobalt carbide. Higher content of metallic cobalt could increase the CO conversion. In addition to the cobalt carbide, carbon fibers were also deposited on the catalyst's surface due to the decomposition of methane at higher carbidation temperatures. Deposited carbon could block the active sites and reduce the contact possibility between the reactant gas and the active sites, thus leading to a lower conversion. By increasing the carbidation temperature from 300 °C to 800 °C, the content of products in the form of liquid decreased from 23% to 4%. It seems that the cobalt carbides were acting as an intermediate and reacting with hydrogen to form methylene as a chain-growth monomer for the formation of long-chain hydrocarbons. Therefore, the catalysts with higher cobalt carbide content had a higher selectivity for the heavier hydrocarbons (liquid products) (Figure 5a).

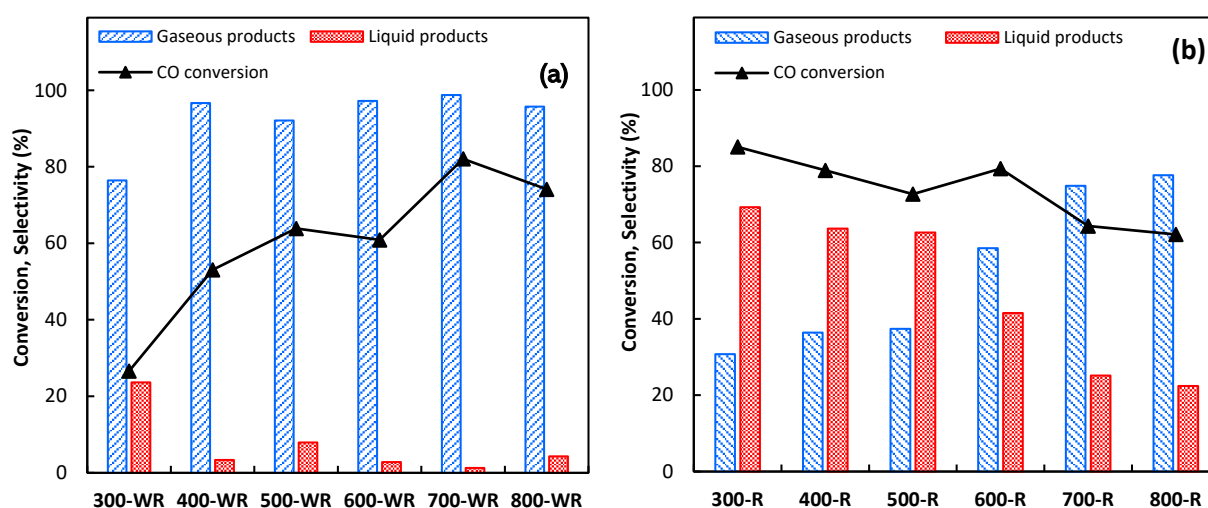


Figure 5. The gaseous and liquid product distributions after FT reaction at 230 °C and 6 h of reaction (a) without reduction with H₂, (b) reduced with H₂ (WR: without reduction step, R: with reduction step).

During the FT reaction over non-reduced catalysts, the content of formed light alkenes was very low and negligible (maximum 1.3% over 300-WR catalyst), whereas alkanes (56.4%) and CO₂ (42.3%) were the main products of the reaction (Figure 6a-WR). The slightly higher alkene formation for the catalysts with lower carbidation temperature could be attributed to the presence of more Co₂C on the surface of the catalysts [9,64]. By increasing the carbidation temperature, the selectivity to CO₂ decreased and reached 10.7% over the 800-WR catalyst, and alkanes selectivity increased to 89%. Methane was the main produced alkane with the selectivity of 97% for the 300-WR. It was decreased to 73% for 400-WR, then again increased gradually to 97% for the 800-WR catalyst (Figure 6b-WR). Formed alkenes are negligible, and propylene was the main formed alkene in gaseous products of the reaction (Figure 6c-WR). Co₂C with (111) facet and nanosphere-like particles could lead to lower activity and higher methane selectivity [10,13,18]. Moreover, during the FT reaction, some portion of deposited graphitic carbon could also be converted to methane through a hydrogenation reaction. This could be the reason for the increase in the methane content in the catalysts with higher graphitic carbon on their surface. The catalysts prepared at 300 °C and 400 °C with the higher content of Co₂C(111) showed lower CO conversion, whereas increasing the Co⁰ content at the catalysts prepared at higher temperatures resulted in a lower CO₂ and alkane (mainly methane) selectivity.

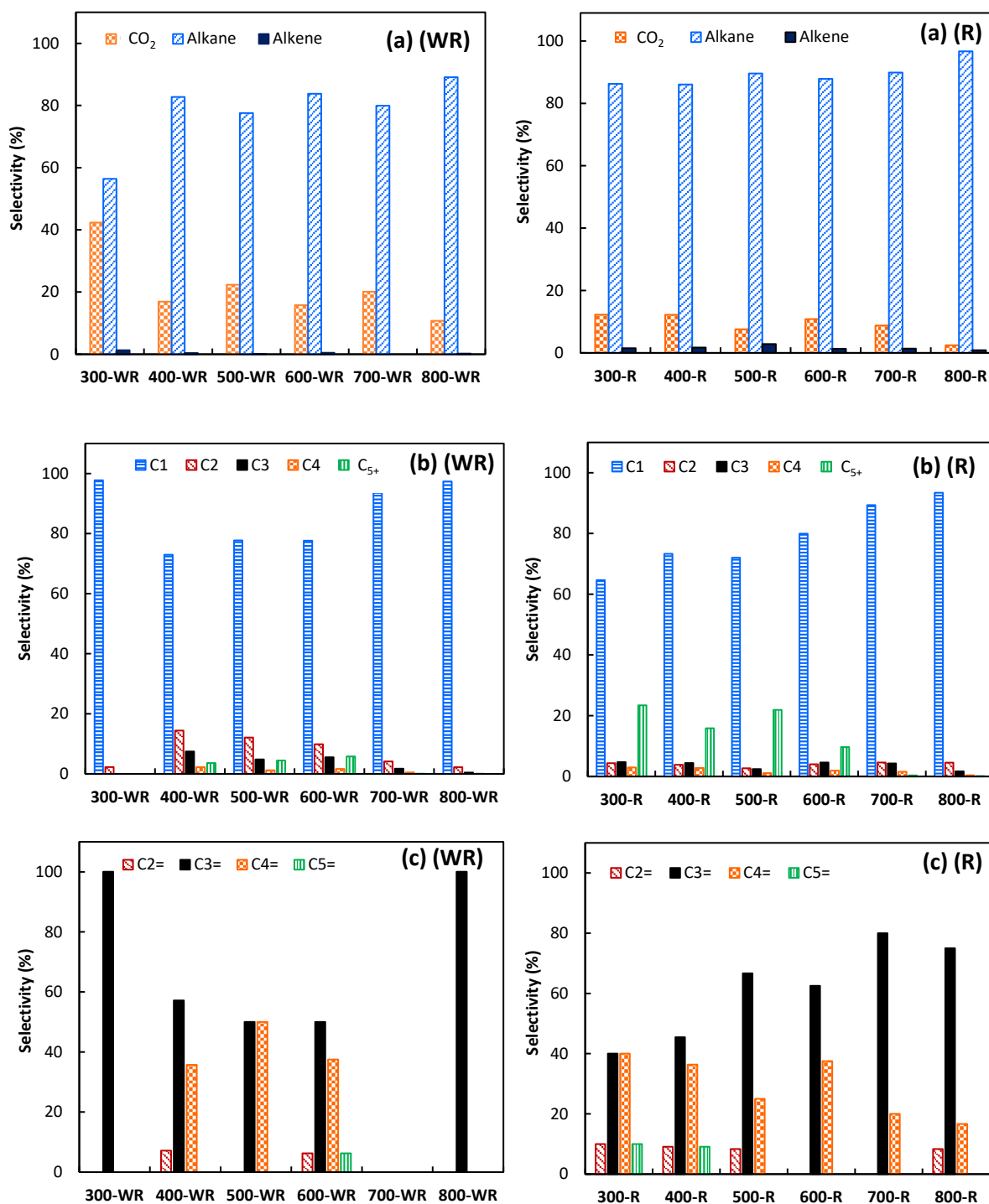


Figure 6. Gaseous product distribution in the FT reaction carbide catalysts: (a) hydrocarbon distribution, (b) alkanes distribution, and (c) alkenes distribution (WR: without reduction step, R: with reduction step).

In the presence of hydrogen, cobalt carbides could be transformed into the face centered-cubic (fcc) and hexagonal close-packed (hcp) Co⁰, which are more efficient for the dissociative adsorption of CO during the FT reaction, and hcp cobalt nanoparticles reported to have higher activity compared with fcc cobalt in the FT reaction [65–67]. The reaction route is also reported to be different over these two different Co crystallographic structures, and the direct dissociation of CO (CO* + H → C* + O* + H*) is preferred over hcp Co, whereas H-assisted dissociation (CO* + H* → CHO* → CH* + O*) is the main mechanism

over fcc cobalt [67]. In order to investigate the stability of the cobalt carbides in the presence of hydrogen and evaluation of the catalytic performances of catalysts after reduction with hydrogen, the FT reactions in an autoclave reactor were repeated, while the catalysts were first reduced under H_2 at $300\text{ }^\circ\text{C}$ for 5 h. Then, the FT reaction was performed at $230\text{ }^\circ\text{C}$ for 6 h (Figures 5 and 6). Results of the FT reaction in an autoclave reactor revealed that CO and H_2 conversions gradually decreased by increasing the catalyst carbidation temperature. The distribution of gaseous and liquid products is shown in Figure 5b.

Over the reduced catalysts, the products shifted from heavier hydrocarbons to lighter hydrocarbons by increasing the carbidation temperature, which was attributed to the content of metallic cobalt in these catalysts. The higher catalytic activity over the 300-R catalyst (which means the catalyst was prepared at the carbidation temperature of $300\text{ }^\circ\text{C}$ and used in the FT reaction after reducing with H_2) could be due to the formation of more metallic cobalt during the reduction step. This provided more active sites for CO dissociation and the production of heavier hydrocarbons. The content of the products in the form of liquid was higher for the FT reaction over the 300-R catalyst. The catalyst activity and production of heavier hydrocarbons in the liquid phase decreased gradually by increasing the carbidation temperature. Compared with the FT reaction without the reduction step, the FT reactions over the reduced catalysts resulted in the formation of a lower amount of CO_2 and methane (Figure 6a-R).

The formation of methane gradually increased from 64% to 93% by increasing the carbidation temperature from $300\text{ }^\circ\text{C}$ to $800\text{ }^\circ\text{C}$, and at the same time, the selectivity to C_{5+} in the gaseous phase decreased (Figure 6b-R). The presence of more cobalt carbides in the catalysts with lower carbidation temperatures resulted in the formation of more metallic cobalt during reduction by hydrogen, which can enhance the CO dissociation and result in higher activity and selectivity to heavier hydrocarbons. Like the non-reduced catalyst, the main formed alkene was propylene over the reduced catalysts, and its content increased by increasing the carbidation temperature (Figure 6c-R). The Co^0 could be carburized in the presence of pure CO and produce Co_2C [68]. However, during the FT reaction, in the presence of CO and H_2 , both Co^0 and Co_2C were found to exist. Therefore, both of them can affect the reaction. During the initial reaction stage, the presence of Co^0 in the reduced catalyst led to a higher selectivity for heavier hydrocarbons and a lower CH_4 and CO_2 selectivity. It has been reported that the higher Co_2C content leads to a high methane selectivity and a lower CO conversion [1,69]. Zhong et al. [10] prepared the Co_2C nanospheres to evaluate their activity for the FT reaction. The CO conversion over the Co_2C nanoparticles was about 10%. High selectivity to methane (~80%), C_2 - C_4 alkanes of ~18%, and the C_2 - C_4 alkenes selectivity of about 2% were obtained during the reaction at $250\text{ }^\circ\text{C}$, 1 bar, and $H_2/CO = 2$. During the FT reaction over the CoMn catalyst, Co^0 was transformed to Co_2C , and the CoMn, which initially existed as $Co_xMn_{1-x}O$, was segregated into Co_2C and MnO. The Co_2C formed during the reaction resulted in higher activity and more light olefins formation. As the reaction proceeded, the formation of C_{5+} and oxygenates decreased.

The evaluation of the liquid phase products for both series of FT reactions (without and with reduction step) showed that the products were a combination of alkanes, alkenes, and a negligible amount of other products such as toluene, and ethylbenzene and propylbenzene were the main products of the FT reaction without the reduction step (Figure 7). The liquid product of the FT reaction with the reduction step consisted of a slightly higher amount of other products (including some oxygenates such as diphenyl ether, acetic anhydride, and dicyclohexyl). The formation of oxygenates was not observed over the catalysts without the reduction step. A small amount of the cyclic products could be due to the reaction of cyclohexane, which was used as the solvent for the FT reaction in the autoclave reactor. The nondissociative adsorption of CO and its insertion into hydrocarbons could result in the formation of oxygenates, which can be converted to alcohol by going through the further hydrogenation process. The FT reaction over carbide catalysts without reduction resulted

in the formation of alkanes in the range of C₄-C₂₂, and the lower carbidation temperature led to the formation of slightly lighter hydrocarbons.

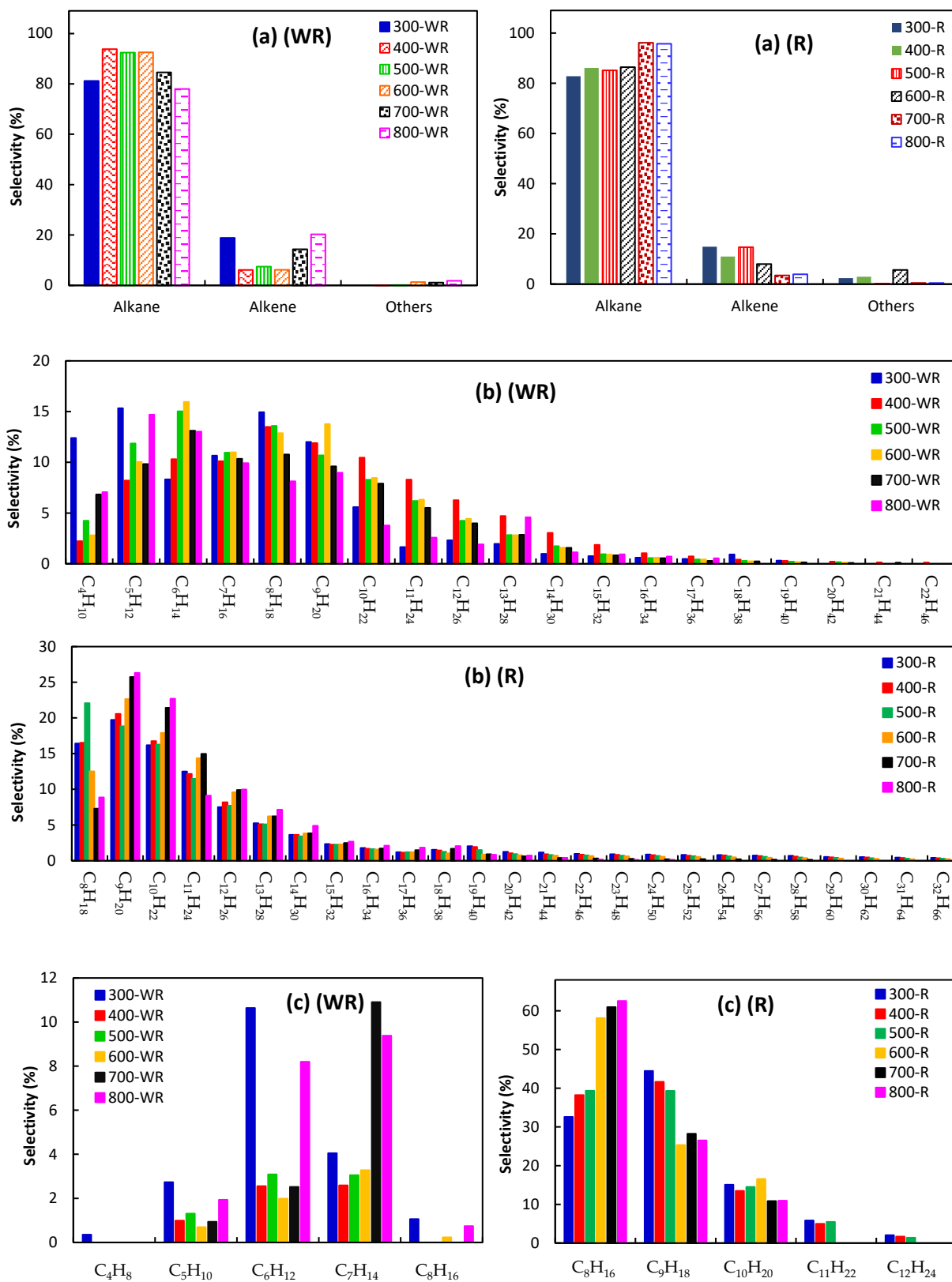


Figure 7. (a) Product distribution in liquid phase products, (b) distribution of n-alkanes, and (c) alkenes in the liquid phase products (WR: without reduction step, R: with reduction step).

By increasing the carbidation temperature, products shifted slightly to heavier hydrocarbons. As expected, the FT reaction over the reduced catalysts resulted in the formation of heavier hydrocarbons in the range of C₈–C₃₂, which could be due to the presence of more active metallic cobalt with higher activity and selectivity to heavy hydrocarbons. The formed alkenes were in the range of C₄–C₈ over carbide catalysts without reduction, whereas heavier alkenes (C₈–C₁₂) were formed over the reaction of reduced catalysts. According to the density functional theory calculations, the active sites for the CO nondissociative adsorption are provided by Co₂C. Co⁰ provides the active sites for CO dissociative adsorption; the insertion of CO to hydrocarbon for oxygenates at the interface of Co and Co₂C is facilitated [19]. In the presence of pure H₂, Co₂C could preserve its activity until 150 °C, whereas at higher temperatures, it starts to decompose to the fcc and hcp Co⁰ and C. At temperatures above 300 °C, Co₂C is completely decomposed [19]. Due to the presence of both H₂ and CO during the FT reaction, cobalt in the form of both Co⁰ and Co₂C existed in the catalyst. The presence of Co⁰ could be beneficial for the production of heavier hydrocarbons. The FT reaction over the reduced catalysts prepared at lower carbidation temperature (with more carbides and less carbon formed on the surface) showed a higher selectivity to heavier hydrocarbons.

3. Materials and Methods

3.1. Catalyst Preparation

The 5%Co/Al₂O₃, 5%Fe/Al₂O₃, and 2.5%Fe2.5%Co/Al₂O₃ as precursors were prepared in advance using the incipient wetness impregnation (IWI) method. First, the required amount of cobalt nitrate hexahydrate (Lech-Ner s.r.o., p.a. purity) was dissolved in deionized water. Then, this solution was added dropwise to the Al₂O₃ support (SASOL, alumina balls with 2.5 mm diameter) at room temperature and under continuous stirring for 1 h. The mixture was then dried at 120 °C overnight. The dried samples were used as precursors in the carbidation step. Prior to the carbidation step, the precursors were preheated at 200 °C for 12 h under N₂ atmosphere (75 cm³/min). For the preparation of carbide catalysts, 4 g of the prepared precursor was exposed to a gas containing 20% CH₄ in H₂ with the flow rate of 300 cm³/min for 3 h at different temperatures in the range of 300 °C to 800 °C. After the carbidation step, catalysts were purged with N₂ for 30 min and passivated for 2 h under 1% O₂ in Ar with a flow rate of 75 cm³/h.

3.2. Catalyst Characterizations

The scanning electron microscope (SEM) (JEOL JSM-IT500HR; JEOL Ltd., Tokyo, Japan) was used to study the surface morphology of the prepared catalysts. Representative backscattered electron or secondary electron images of microstructures were taken in high vacuum mode, using an accelerating voltage of 15 kV. An inductively coupled plasma-optical emission spectrometer (ICP-OES; Agilent 725/Agilent Technologies Inc., Santa Clara, CA, USA) was used for the determination of the bulk metal content in the prepared catalysts. X-ray diffraction (XRD) was used to determine the type of phases and crystallinity of the catalysts using a D8 Advance ECO (Bruker AXS GmbH, Karlsruhe, Germany) with CuK α radiation ($\lambda = 1.5406 \text{ \AA}$). The step time of 0.5 s and the step size of 0.02° in a 2 θ angle ranging from 10° to 70° were used for XRD analysis. X-ray photoelectron spectroscopy (XPS) spectra of the samples were obtained using the XPS instrument in a high-vacuum chamber, which was equipped with a source SPECS X-ray XR50 (SPECS Surface Nano Analysis GmbH, Germany), where an Al anode (1486.6 eV) and a Mg anode (1253.6 eV) were used, and with a hemispherical analyzer SPECS PHOIBOS 100 with a five-channel detector. Thermo Scientific™ Avantage Software was used for XPS data processing. The Raman analysis for the samples was performed using a DXR (Thermo Fischer Scientific, Waltham, MA, USA) Raman microscope. The laser beam was focused onto the catalyst surface using an optical microscope with a magnification of 10 \times . A 532 nm laser with an exposure time of 7 s and a power of 9 mW was used for sample excitation. Analyses were performed in the area of 100–3400 cm⁻¹.

3.3. Catalyst Evaluation

The FT reaction was performed in a 1 L stainless steel autoclave reactor (Parr instruments). In a typical experiment, 1.5 g of catalyst and 35 mL of cyclohexane as a solvent were added to the reactor vessel. The reactor temperature was increased to 230 °C (3 °C/min) and pressurized to 5 MPa with syngas ($H_2/CO = 2$). The reaction was conducted in batch mode for 6 h under constant stirring of 800 rpm to eliminate the diffusion control region. The conversion rate was measured according to the decrease in pressure during the reaction and the composition of the reactant gas before and after the reaction. For the FT reaction with the in situ catalyst reduction, the reactor was heated to 300 °C (3 °C/min) and then pressurized with H_2 to 5 MPa for 5 h. After reduction, the reactor system was cooled to room temperature, and the gas was switched to syngas ($H_2/CO = 2$). The FT reaction was performed at 230 °C and 5 MPa for 6 h. After the termination of the reaction, the gaseous and liquid products were analyzed using different chromatographic procedures. The resultant gas sample was transferred to a gas bag and analyzed with a gas chromatograph, the Agilent 7890A, with three parallel channels that collected data simultaneously. The channels are equipped with two thermal conductivity detectors (TCD), CO , H_2 , N_2 , and CO_2 gases, and a flame ionization detector (FID) to detect hydrocarbons. The liquid samples were analyzed using Thermo Scientific ITQ Series GC/MS Ion Trap Mass Spectrometers.

4. Conclusions

Cobalt-based catalysts with high activity and selectivity to long-chain hydrocarbons are widely used for this reaction. Identification of the active phase could be beneficial in enhancing the product yield of the FT reaction. A series of FT reactions were performed in an autoclave reactor to evaluate the catalytic activity of cobalt carbide catalysts and their role in the product distribution during the FT reaction. CoC_x/Al_2O_3 catalysts were prepared by carbidation of Co/Al_2O_3 catalysts at different temperatures and over 20% CH_4 in an H_2 gas stream. Different characterization methods confirmed the presence of Co_2C . By increasing the carbidation temperature, the content of Co_2C decreased, whereas the Co^0 content increased by temperature. The Co/Al_2O_3 catalyst was also active for the methane decomposition to hydrogen and graphitic carbon at higher carbidation temperatures. Cobalt carbides were unstable in the presence of hydrogen at high temperatures and decomposed to metallic cobalt and carbon, which resulted in the increase of metallic cobalt's content. The catalysts with higher cobalt carbide had the lowest CO conversion of 26%, which then increased to 74% for the catalyst with lower Co_2C content prepared at 800 °C. The main products were light alkanes in the range of C_1 – C_5 (mainly methane), and the heavier hydrocarbons (in the range of C_4 – C_{22}) decreased from 23% to 4%. By increasing the carbidation temperature, the Co_2C content decreased, and the metallic cobalt content increased, which resulted in higher catalytic activity. At the same time, the selectivity to CO_2 decreased. The $Co_2C(111)$ facet with the nanosphere-like particles showed a lower activity and higher methane selectivity under mild FT reaction conditions. The formation of alkenes was negligible over these carbide catalysts, which could be due to the lower content of Co_2C nanoprisms with specific exposed facets of (101) and (020); these are known as the FTO active phase, with higher activity for CO hydrogenation and lower methane selectivity. In addition, a series of FT reactions were performed over the carbide catalyst with a prior reduction step using pure hydrogen at 300 °C. These reduced catalysts showed a different catalytic performance. The main products were the heavier hydrocarbons (C_8 – C_{32}) with 69%. By increasing the carbidation temperature to 800 °C, the content of liquid products decreased to 22%, whereas the light hydrocarbons content increased to 78%. The CO conversion decreased by increasing the carbidation temperature in the reduced catalysts. For the catalysts prepared at higher temperatures, the presence of lower Co_2C , which is transformed into hcp cobalt during the reduction with hydrogen, as well as the presence of lower metallic fcc cobalt, resulted in lower CO conversion and less heavy hydrocarbons.

Supplementary Materials: The following supporting information can be downloaded at: <https://www.mdpi.com/article/10.3390/catal12101222/s1>, Figure S1: Survey XPS spectra scan of carbide catalysts, Figure S2: Carbon motions in the D and G modes [45].

Author Contributions: Conceptualization, Z.G. and Z.T.; methodology, Z.G.; validation, Z.G., Z.T. and F.G.; formal analysis, Z.G., Z.T., E.S., I.H., N.S.; investigation, Z.G., Z.T., E.S., I.H., N.S. and F.G.; data curation, Z.G., Z.T., E.S., I.H., N.S.; writing—original draft preparation, Z.G., Z.T., F.G.; writing—review and editing, Z.G., Z.T., F.G.; visualization, Z.G.; supervision, Z.G., Z.T. All authors have read and agreed to the published version of the manuscript.

Funding: The publication is a result of the project which was carried out within the financial support of the Ministry of Industry and Trade of the Czech Republic with institutional support for long-term conceptual development of research organization. The result was achieved using the infrastructure included in the project Efficient Use of Energy Resources Using Catalytic Processes (LM2018119), which has been financially supported by MEYS within the targeted support of large infrastructures.

Data Availability Statement: MDPI Research Data Policies.

Conflicts of Interest: The authors declare no conflict of interest. The funders had no role in the design of the study; in the collection, analyses, or interpretation of data; in the writing of the manuscript, or in the decision to publish the results.

References

1. Mohandas, J.C.; Gnanamani, M.K.; Jacobs, G.; Ma, W.; Ji, Y.; Khalid, S.; Davis, B.H. Fischer–Tropsch synthesis: Characterization and reaction testing of cobalt carbide. *ACS Catal.* **2011**, *1*, 1581–1588. [[CrossRef](#)]
2. Kwak, G.; Woo, M.H.; Kang, S.C.; Park, H.-G.; Lee, Y.-J.; Jun, K.-W.; Ha, K.-S. In situ monitoring during the transition of cobalt carbide to metal state and its application as Fischer–Tropsch catalyst in slurry phase. *J. Catal.* **2013**, *307*, 27–36. [[CrossRef](#)]
3. Lin, Q.; Liu, B.; Jiang, F.; Fang, X.; Xu, Y.; Liu, X. Assessing the formation of cobalt carbide and its catalytic performance under realistic reaction conditions and tuning product selectivity in a cobalt-based FTS reaction. *Catal. Sci. Technol.* **2019**, *9*, 3238–3258. [[CrossRef](#)]
4. Gholami, Z.; Tišler, Z.; Rubáš, V. Recent advances in Fischer–Tropsch synthesis using cobalt-based catalysts: A review on supports, promoters, and reactors. *Catal. Rev.* **2021**, *63*, 512–595. [[CrossRef](#)]
5. Claeys, M.; Dry, M.E.; van Steen, E.; du Plessis, E.; van Berge, P.J.; Saib, A.M.; Moodley, D.J. In situ magnetometer study on the formation and stability of cobalt carbide in Fischer–Tropsch synthesis. *J. Catal.* **2014**, *318*, 193–202. [[CrossRef](#)]
6. Yang, X.; Yang, J.; Zhao, T.; Qian, W.; Wang, Y.; Holmen, A.; Jiang, W.; Chen, D.; Ben, H. Kinetic insights into the effect of promoters on Co/Al₂O₃ for Fischer–Tropsch synthesis. *Chem. Eng. J.* **2022**, *445*, 136655. [[CrossRef](#)]
7. Karaca, H.; Safonova, O.V.; Chambrey, S.; Fongarland, P.; Roussel, P.; Griboval-Constant, A.; Lacroix, M.; Khodakov, A.Y. Structure and catalytic performance of Pt-promoted alumina-supported cobalt catalysts under realistic conditions of Fischer–Tropsch synthesis. *J. Catal.* **2011**, *277*, 14–26. [[CrossRef](#)]
8. Cheng, J.; Hu, P.; Ellis, P.; French, S.; Kelly, G.; Lok, C.M. Density functional theory study of iron and cobalt carbides for Fischer–Tropsch synthesis. *J. Phys. Chem. C* **2010**, *114*, 1085–1093. [[CrossRef](#)]
9. Li, Z.; Zhong, L.; Yu, F.; An, Y.; Dai, Y.; Yang, Y.; Lin, T.; Li, S.; Wang, H.; Gao, P.; et al. Effects of sodium on the catalytic performance of CoMn catalysts for Fischer–Tropsch to olefin reactions. *ACS Catal.* **2017**, *7*, 3622–3631. [[CrossRef](#)]
10. Zhong, L.; Yu, F.; An, Y.; Zhao, Y.; Sun, Y.; Li, Z.; Lin, T.; Lin, Y.; Qi, X.; Dai, Y.; et al. Cobalt carbide nanoprisms for direct production of lower olefins from syngas. *Nature* **2016**, *538*, 84–87. [[CrossRef](#)]
11. Xiang, Y.; Kruse, N. Tuning the catalytic CO hydrogenation to straight- and long-chain aldehydes/alcohols and olefins/paraffins. *Nat. Commun.* **2016**, *7*, 13058. [[CrossRef](#)] [[PubMed](#)]
12. Gnanamani, M.K.; Jacobs, G.; Shafer, W.D.; Sparks, D.E.; Hopps, S.; Thomas, G.A.; Davis, B.H. Low temperature water–gas shift reaction over alkali metal promoted cobalt carbide catalysts. *Top. Catal.* **2014**, *57*, 612–618. [[CrossRef](#)]
13. Lin, T.; Yu, F.; An, Y.; Qin, T.; Li, L.; Gong, K.; Zhong, L.; Sun, Y. Cobalt carbide nanocatalysts for efficient syngas conversion to value-added chemicals with high selectivity. *Acc. Chem. Res.* **2021**, *54*, 1961–1971. [[CrossRef](#)] [[PubMed](#)]
14. Lin, T.; Qi, X.; Wang, X.; Xia, L.; Wang, C.; Yu, F.; Wang, H.; Li, S.; Zhong, L.; Sun, Y. Direct production of higher oxygenates by syngas conversion over a multifunctional catalyst. *Angew. Chem. Int. Ed.* **2019**, *58*, 4627–4631. [[CrossRef](#)] [[PubMed](#)]
15. Chen, W.; Pilot, I.A.W.; Pestman, R.; Hensen, E.J.M. Mechanism of cobalt-catalyzed CO hydrogenation: 2. Fischer–Tropsch synthesis. *ACS Catal.* **2017**, *7*, 8061–8071. [[CrossRef](#)]
16. Gholami, Z.; Gholami, F.; Tišler, Z.; Hubáček, J.; Tomas, M.; Bačiak, M.; Vakili, M. Production of light olefins via Fischer–Tropsch process using iron-based catalysts: A review. *Catalysts* **2022**, *12*, 174. [[CrossRef](#)]
17. Davis, B.H.; Ocelli, M.L. *Advances in Fischer–Tropsch Synthesis, Catalysts, and Catalysis*, 1st ed.; CRC press: Boca, Raton, 2009. [[CrossRef](#)]

18. Xiao, Y.; Sun, P.; Cao, M. Core–Shell bimetallic carbide nanoparticles confined in a three-dimensional N-doped carbon conductive network for efficient lithium storage. *ACS Nano* **2014**, *8*, 7846–7857. [[CrossRef](#)]
19. Pei, Y.-P.; Liu, J.-X.; Zhao, Y.-H.; Ding, Y.-J.; Liu, T.; Dong, W.-D.; Zhu, H.-J.; Su, H.-Y.; Yan, L.; Li, J.-L.; et al. High alcohols synthesis via Fischer–Tropsch reaction at cobalt metal/carbide interface. *ACS Catal.* **2015**, *5*, 3620–3624. [[CrossRef](#)]
20. Moya-Cancino, J.G.; Honkanen, A.-P.; van der Eerden, A.M.J.; Oord, R.; Monai, M.; ten Have, I.; Sahle, C.J.; Meirer, F.; Weckhuysen, B.M.; de Groot, F.M.F.; et al. In Situ X-ray Raman scattering spectroscopy of the formation of cobalt carbides in a Co/TiO₂ Fischer–Tropsch synthesis catalyst. *ACS Catal.* **2021**, *11*, 809–819. [[CrossRef](#)]
21. Osa, A.R.; Lucas, A.; Valverde, J.; Romero, A.; Monteagudo, I.; Coca, P.; Sánchez, P. Influence of alkali promoters on synthetic diesel production over Co catalyst. *Catal. Today* **2011**, *167*, 96–106. [[CrossRef](#)]
22. Lu, M.; Fatah, N.; Khodakov, A.Y. Optimization of solvent-free mechanochemical synthesis of Co/Al₂O₃ catalysts using low- and high-energy processes. *J. Mater. Sci.* **2017**, *52*, 12031–12043. [[CrossRef](#)]
23. Peña, D.; Griboval-Constant, A.; Lecocq, V.; Diehl, F.; Khodakov, A.Y. Influence of operating conditions in a continuously stirred tank reactor on the formation of carbon species on alumina supported cobalt Fischer–Tropsch catalysts. *Catal. Today* **2013**, *215*, 43–51. [[CrossRef](#)]
24. Yi, J.-H.; Sun, Y.-Y.; Gao, J.-F.; Xu, C.-Y. Synthesis of crystalline γ -Al₂O₃ with high purity. *Trans. Nonferrous Met. Soc. China* **2009**, *19*, 1237–1242. [[CrossRef](#)]
25. Choi, Y.I.; Yang, J.H.; Park, S.J.; Sohn, Y. Energy storage and CO₂ reduction performances of Co/Co₂C/C prepared by an anaerobic ethanol oxidation reaction using sacrificial SnO₂. *Catalysts* **2020**, *10*, 1116. [[CrossRef](#)]
26. Xia, S.-G.; Zhang, Z.; Wu, J.-N.; Wang, Y.; Sun, M.-J.; Cui, Y.; Zhao, C.-L.; Zhong, J.-Y.; Cao, W.; Wang, H.; et al. Cobalt carbide nanosheets as effective catalysts toward photothermal degradation of mustard-gas simulants under solar light. *Appl. Catal. B Environ.* **2021**, *284*, 119703. [[CrossRef](#)]
27. Petersen, A.P.; Claeys, M.; Kooyman, P.J.; van Steen, E. Cobalt-based Fischer–Tropsch synthesis: A kinetic evaluation of metal–support interactions using an inverse model system. *Catalysts* **2019**, *9*, 794. [[CrossRef](#)]
28. van Ravenhorst, I.K.; Hoffman, A.S.; Vogt, C.; Boubnov, A.; Patra, N.; Oord, R.; Akatay, C.; Meirer, F.; Bare, S.R.; Weckhuysen, B.M. On the cobalt carbide formation in a Co/TiO₂ Fischer–Tropsch synthesis catalyst as studied by high-pressure, long-term operando X-ray absorption and diffraction. *ACS Catal.* **2021**, *11*, 2956–2967. [[CrossRef](#)]
29. Nuernberg, G.B.; Fajardo, H.V.; Mezalira, D.Z.; Casarin, T.J.; Probst, L.F.D.; Carreño, N.L.V. Preparation and evaluation of Co/Al₂O₃ catalysts in the production of hydrogen from thermo-catalytic decomposition of methane: Influence of operating conditions on catalyst performance. *Fuel* **2008**, *87*, 1698–1704. [[CrossRef](#)]
30. Gao, B.; Wang, I.W.; Ren, L.; Haines, T.; Hu, J. Catalytic performance and reproducibility of Ni/Al₂O₃ and Co/Al₂O₃ mesoporous aerogel catalysts for methane decomposition. *Ind. Eng. Chem. Res.* **2019**, *58*, 798–807. [[CrossRef](#)]
31. Fakeeha, A.H.; Ibrahim, A.A.; Khan, W.U.; Abasaeed, A.E.; Al-Fatesh, A.S. Hydrogen production by catalytic methane decomposition over Ni, Co, and Ni-Co/Al₂O₃ catalyst. *Pet. Sci. Technol.* **2016**, *34*, 1617–1623. [[CrossRef](#)]
32. Saraswat, S.K.; Pant, K. Progressive loading effect of Co Over SiO₂/Al₂O₃ catalyst for CO_x free hydrogen and carbon nanotubes production via catalytic decomposition of methane. *Int. J. Chem. Mol. Eng.* **2015**, *9*, 485–489. [[CrossRef](#)]
33. Koerts, T.; Deelen, M.J.A.G.; van Santen, R.A. Hydrocarbon formation from methane by a low-temperature two-step reaction sequence. *J. Catal.* **1992**, *138*, 101–114. [[CrossRef](#)]
34. Narkiewicz, U.; Podsiadły, M.; Jędrzejewski, R.; Pelech, I. Catalytic decomposition of hydrocarbons on cobalt, nickel and iron catalysts to obtain carbon nanomaterials. *Appl. Catal. A Gen.* **2010**, *384*, 27–35. [[CrossRef](#)]
35. Pang, H.; Wang, X.; Zhang, G.; Chen, H.; Lv, G.; Yang, S. Characterization of diamond-like carbon films by SEM, XRD and Raman spectroscopy. *Appl. Surf. Sci.* **2010**, *256*, 6403–6407. [[CrossRef](#)]
36. Matveev, V.V.; Baranov, D.A.; Yurkov, G.Y.; Akatiev, N.G.; Dotsenko, I.P.; Gubin, S.P. Cobalt nanoparticles with preferential hcp structure: A confirmation by X-ray diffraction and NMR. *Chem. Phys. Lett.* **2006**, *422*, 402–405. [[CrossRef](#)]
37. Paterson, J.; Peacock, M.; Ferguson, E.; Purves, R.; Ojeda, M. In situ diffraction of Fischer–Tropsch catalysts: Cobalt reduction and carbide formation. *Chem. Cat. Chem.* **2017**, *9*, 3463–3469. [[CrossRef](#)]
38. Kumar, C.V.; Pattammattel, A. Chapter 3-Characterization techniques for graphene. In *Introduction to Graphene*; Kumar, C.V., Pattammattel, A., Eds.; Elsevier: Amsterdam, The Netherlands, 2017; pp. 45–74.
39. Fang, H.; Huang, T.; Sun, Y.; Kang, B.; Liang, D.; Yao, S.; Yu, J.; Dinesh, M.M.; Wu, S.; Lee, J.Y.; et al. Metal-organic framework-derived core-shell-structured nitrogen-doped CoC_x/FeCo@C hybrid supported by reduced graphene oxide sheets as high performance bifunctional electrocatalysts for ORR and OER. *J. Catal.* **2019**, *371*, 185–195. [[CrossRef](#)]
40. Xiong, J.; Ding, Y.; Wang, T.; Yan, L.; Chen, W.; Zhu, H.; Lu, Y. The formation of Co₂C species in activated carbon supported cobalt-based catalysts and its impact on Fischer–Tropsch reaction. *Catal. Lett.* **2005**, *102*, 265–269. [[CrossRef](#)]
41. Li, S.; Yang, C.; Yin, Z.; Yang, H.; Chen, Y.; Lin, L.; Li, M.; Li, W.; Hu, G.; Ma, D. Wet-chemistry synthesis of cobalt carbide nanoparticles as highly active and stable electrocatalyst for hydrogen evolution reaction. *Nano Res.* **2017**, *10*, 1322–1328. [[CrossRef](#)]
42. Zhang, T.; Wu, J.; Xu, Y.; Wang, X.; Ni, J.; Li, Y.; Niemantsverdriet, J.W. Cobalt and cobalt carbide on alumina/NiAl(110) as model catalysts. *Catal. Sci. Technol.* **2017**, *7*, 5893–5899. [[CrossRef](#)]
43. Bayer, B.C.; Bosworth, D.A.; Michaelis, F.B.; Blume, R.; Habler, G.; Abart, R.; Weatherup, R.S.; Kidambi, P.R.; Baumberg, J.J.; Knop-Gericke, A.; et al. In situ observations of phase transitions in metastable nickel (carbide)/carbon nanocomposites. *J. Phys. Chem. C* **2016**, *120*, 22571–22584. [[CrossRef](#)] [[PubMed](#)]

44. Sarr, M.; Bahlawane, N.; Arl, D.; Dossot, M.; McRae, E.; Lenoble, D. Tailoring the properties of atomic layer deposited nickel and nickel carbide thin films via chain-length control of the alcohol reducing agents. *J. Phys. Chem. C* **2014**, *118*, 23385–23392. [[CrossRef](#)]
45. Ferrari, A.C.; Robertson, J. Interpretation of Raman spectra of disordered and amorphous carbon. *Phys. Rev. B* **2000**, *61*, 14095. [[CrossRef](#)]
46. Sfyris, D.; Sfyris, G.; Galiotis, C. Stress interpretation of graphene E-2g and A-1g vibrational modes: Theoretical analysis. *arXiv* **2017**, arXiv:1706.04465. [[CrossRef](#)]
47. Tembre, A.; Hénoque, J.; Clin, M. Infrared and Raman spectroscopic study of carbon-cobalt composites. *Int. J. Spectrosc.* **2011**, *2011*, 186471. [[CrossRef](#)]
48. Issi, J.-P.; Araujo, P.T.; Dresselhaus, M.S. Electron and phonon transport in graphene in and out of the bulk. In *Physics of Graphene*; Aoki, H., Dresselhaus, M.S., Eds.; Springer International Publishing: Cham, Switzerland, 2014; pp. 65–112. [[CrossRef](#)]
49. Diallo, A.; Beye, A.C.; Doyle, T.B.; Park, E.; Maaza, M. Green synthesis of Co₃O₄ nanoparticles via *Aspalathus linearis*: Physical properties. *Green Chem. Lett. Rev.* **2015**, *8*, 30–36. [[CrossRef](#)]
50. Rashad, M.; Rüsing, M.; Berth, G.; Lischka, K.; Pawlis, A. CuO and Co₃O₄ nanoparticles: Synthesis, characterizations, and Raman spectroscopy. *J. Nanomater.* **2013**, *2013*. [[CrossRef](#)]
51. Jiang, J.; Li, L. Synthesis of sphere-like Co₃O₄ nanocrystals via a simple polyol route. *Mater. Lett.* **2007**, *61*, 4894–4896. [[CrossRef](#)]
52. Hadjiev, V.G.; Iliev, M.N.; Vergilov, I.V. The Raman spectra of Co₃O₄. *J. Phys. C Solid State Phys.* **1988**, *21*, L199–L201. [[CrossRef](#)]
53. Maaz, K. *Cobalt*; IntechOpen: London, UK, 2017; Available online: <https://www.intechopen.com/books/6133> (accesses on 21 July 2022).
54. Rivas-Murias, B.; Salgueiriño, V. Thermodynamic CoO–Co₃O₄ crossover using Raman spectroscopy in magnetic octahedron-shaped nanocrystals. *J. Raman Spectrosc.* **2017**, *48*, 837–841. [[CrossRef](#)]
55. Xiao, T.-C.; York, A.P.E.; Al-Megren, H.; Williams, C.V.; Wang, H.-T.; Green, M.L.H. Preparation and characterisation of bimetallic cobalt and molybdenum carbides. *J. Catal.* **2001**, *202*, 100–109. [[CrossRef](#)]
56. D'Ippolito, V.; Andreozzi, G.B. Linking crystal chemistry and physical properties of natural and synthetic spinels: An UV-VIS-NIR and Raman study. Ph.D. Thesis, Sapienza Università di Roma, Rome, Italy, 2013.
57. Mashkovtsev, R.I.; Thomas, V.G. Nitrogen atoms encased in cavities within the beryl structure as candidates for qubits. *Appl. Magn. Reson.* **2005**, *28*, 401–409. [[CrossRef](#)]
58. Zhao, Y.; Yamaguchi, Y.; Liu, C.; Sekine, S.; Dou, X. Quantitative detection of ethanol/acetone in complex solutions using Raman spectroscopy based on headspace gas analysis. *Appl. Spectrosc.* **2018**, *72*, 280–287. [[CrossRef](#)] [[PubMed](#)]
59. Hoekstra, J.; Beale, A.M.; Soulimani, F.; Versluijs-Helder, M.; Geus, J.W.; Jenneskens, L.W. Base metal catalyzed graphitization of cellulose: A combined Raman spectroscopy, Temperature-Dependent X-ray Diffraction and High-Resolution Transmission Electron Microscopy Study. *J. Phys. Chem. C* **2015**, *119*, 10653–10661. [[CrossRef](#)]
60. Armenta, S.; Garrigues, S.; de la Guardia, M. Determination of iprodione in agrochemicals by infrared and Raman spectrometry. *Anal. Bioanal. Chem.* **2007**, *387*, 2887–2894. [[CrossRef](#)]
61. Perelygin, I.S.; Itkulov, I.G. Spontaneous raman spectroscopic study of the association of liquid γ -butyrolactone molecules. *J. Struct. Chem.* **1996**, *37*, 928–932. [[CrossRef](#)]
62. Ostrovskii, D.; Edvardsson, M.; Jacobsson, P. Weak polymer–electrolyte interaction revealed by Fermi resonance perturbed Raman bands. *J. Raman Spectrosc.* **2003**, *34*, 40–49. [[CrossRef](#)]
63. Thombare, J.V.; Lohar, G.M.; Shinde, S.K.; Dhasade, S.S.; Rath, M.C.; Fulari, V.J. Synthesis, characterization and surface wettability study of polypyrrole films: Effect of applied constant current density. *Electron. Mater. Lett.* **2015**, *11*, 266–270. [[CrossRef](#)]
64. Dai, Y.; Zhao, Y.; Lin, T.; Li, S.; Yu, F.; An, Y.; Wang, X.; Xiao, K.; Sun, F.; Jiang, Z.; et al. Particle size effects of cobalt carbide for Fischer–Tropsch to olefins. *ACS Catal.* **2019**, *9*, 798–809. [[CrossRef](#)]
65. ten Have, I.C.; Weckhuysen, B.M. The active phase in cobalt-based Fischer–Tropsch synthesis. *Chem. Catal.* **2021**, *1*, 339–363. [[CrossRef](#)]
66. Lyu, S.; Wang, L.; Zhang, J.; Liu, C.; Sun, J.; Peng, B.; Wang, Y.; Rappé, K.G.; Zhang, Y.; Li, J.; et al. Role of active phase in Fischer–Tropsch synthesis: Experimental evidence of CO activation over single-phase cobalt catalysts. *ACS Catal.* **2018**, *8*, 7787–7798. [[CrossRef](#)]
67. Liu, J.-X.; Su, H.-Y.; Sun, D.-P.; Zhang, B.-Y.; Li, W.-X. Crystallographic dependence of CO activation on cobalt catalysts: HCP versus FCC. *J. Am. Chem. Soc.* **2013**, *135*, 16284–16287. [[CrossRef](#)] [[PubMed](#)]
68. Chen, P.-P.; Liu, J.-X.; Li, W.-X. Carbon monoxide activation on cobalt carbide for Fischer–Tropsch synthesis from first-principles theory. *ACS Catal.* **2019**, *9*, 8093–8103. [[CrossRef](#)]
69. Weller, S.; Hofer, L.J.E.; Anderson, R.B. The role of bulk cobalt carbide in the Fischer–Tropsch synthesis. *J. Am. Chem. Soc.* **1948**, *70*, 799–801. [[CrossRef](#)]